Revista Internacional de Métodos Numéricos para Cálculo y Diseño en Ingeniería

ARTICLE

# Dynamic Mechanisms and Multiparameter Control of Fracture-Induced Lost Circulation in Deep Wells—A Fluid-Solid Coupling Approach

**Pan Fu[1,2], Yueyang Guan[1,2], Qi He[1,2], Jiangshuai Wang[3,*] and Bohan Zheng[3]**

[1]CNPC Engineering Technology R&D Company Limited, Beijing, China
[2]National Engineering Research Center of Oil & Gas Drilling and Completion Technology, Beijing, China
[3]School of Petroleum and Natural Gas Engineering, Changzhou University, Changzhou, China
*Corresponding Author: Jiangshuai Wang. Email: wjs125126@163.com

Received: 01 June 2026; Accepted: 04 August 2026

**ABSTRACT:** Deep and ultra-deep well drilling in multi-scale fractured formations frequently encounters fracture-induced lost circulation, which restricts drilling efficiency and reservoir development. To address this problem, this paper establishes a dynamic finite element numerical model based on fluid-solid coupling theory, revealing the multi-physics coupling mechanism of fracture propagation and leakage channel evolution. The model fully considers the seepage-stress coupling effect during drilling fluid circulation, and quantitatively analyzes the influences of pump rate, fluid density, fluid viscosity, fracture geometric parameters, elastic modulus, Poisson's ratio and *in-situ* stress on fracture aperture and fluid loss rate. The research results show that: pump rate and fluid density are positively correlated with loss rate and fracture aperture; fluid viscosity presents two-stage regulation characteristics, which is negatively correlated with leakage parameters at the fracture initiation stage and positively correlated in steady-state leakage stage; longer fracture length increases loss rate but reduces fracture aperture; elastic modulus, Poisson's ratio and *in-situ* stress mainly affect the early leakage behavior, with little influence on steady-state stage. The proposed multi-parameter coupling control model can realize dynamic prediction of multi-fracture leakage in deep wells, and provides theoretical support for on-site anti-leakage and plugging work.

**KEYWORDS:** Lost circulation; multi-scale fractured formations; fluid-solid coupling; dynamic circulation; finite element method

## 1 Introduction

Lost circulation is a common and serious engineering problem in oil and gas drilling and has long been a research hotspot in petroleum engineering. This issue easily induces wellbore instability, gas invasion, and downhole operation failure, increases drilling cost, prolongs the construction cycle, and reduces hydrocarbon recovery efficiency [1,2]. Therefore, accurate prediction and effective control of drilling fluid loss are key technical problems restricting oil and gas exploration and development.

Lost circulation is closely related to formation fracture pressure and natural fracture channels. When bottomhole pressure exceeds formation fracture pressure, rock will fracture to form new leakage channels or expand existing fractures, resulting in a large amount of drilling fluid loss. For naturally fractured formations, a slight bottomhole pressure difference will also trigger leakage, which is defined as fracture-induced lost circulation [3,4]. According to industry statistics, lost circulation occurs in 20%–25% of global drilling operations, with annual remediation costs exceeding 4 billion US dollars [5]. In North American shale gas and carbonate reservoirs, severe lost circulation accounts for 40% of total drilling time [6]; in

Middle Eastern carbonate reservoirs, the incidence of lost circulation is over 30%, and non-productive time caused by leakage exceeds 50% [7].

Existing studies on lost circulation mainly focus on leakage pressure prediction, loss rate calculation, and fracture parameter analysis, and most models adopt single-fracture assumptions.Jia et al. [8] introduced fracture tortuosity to characterize fracture surface roughness, and analyzed the dynamic leakage law under different fracture parameters. Lietard et al. [9] established a radial flow model for high-permeability fractured formations (permeability K > 50 mD), considering dynamic net pressure of fractures, nonlinear variation of fracture width, fluid rheology, and time effect. Li Daqi et al. [10] derived the leakage equation of an infinite single fracture based on Navier-Stokes equations, and quantified the relationship between fracture geometry and fluid filtration. Du et al. [11] Recent advances in quantitative fracture prediction for Tertiary formations have demonstrated the importance of multi-scale fracture characterization for accurate lost circulation forecasting. Lavrov et al. [12,13] coupled the wellbore breathing effect with linear elastic fracture theory to build a two-dimensional plane model. The results show that fracture propagation length, pressure gradient, and fluid thixotropy significantly affect loss rate, and fracture closure is the main reason for leakage termination. However, single-fracture models cannot reflect the actual characteristics of complex fractured formations, leading to limited prediction accuracy.

To make up for the above defects, scholars have carried out numerical simulations on fracture networks and multi-fracture interaction during drilling fluid circulation. Salehi [14] applied a cohesive zone model in hydraulic fracturing simulation, but the constant injection rate boundary condition cannot match the dynamic wellbore pressure in actual drilling. Feng et al. [15,16] established a finite element model coupled with transient bottomhole pressure, which can jointly analyze pressure change, loss rate evolution, and fracture propagation. Zhang Shuai et al. [17] realized multi-physics coupling simulation in ABAQUS, [18] and found that temperature change will induce stress redistribution, change fracture propagation path, and affect loss rate. Nevertheless, current numerical models still fail to fully characterize the heterogeneous fracture network of actual formations. Recent advances in thermo-hydro-mechanical coupling [19], plasma pulse fracturing [20], and fractured reservoir geomechanics [21] provide complementary perspectives on fracture activation and fluid-solid interaction, though their direct application to dynamic lost circulation remains limited.

Aiming at the above research deficiencies, this paper adopts ABAQUS finite element software and combines pipe flow elements and cohesive zone elements to construct a two-dimensional fluid-solid coupling model. The influences of engineering parameters, fracture characteristics, and geomechanical parameters on dynamic leakage behavior and fracture morphology are studied via numerical simulation. The model can accurately reflect the fluid-structure interaction between wellbore flow and fracture deformation, and provide a theoretical basis for risk assessment and leakage control in deep complex fractured formations.

## 2 Basic Theory

### *2.1 Fluid Pipe Element*

Pipe flow elements are used to simulate drilling fluid circulation inside the wellbore and annulus. Assuming the drilling fluid is unidirectional and incompressible, the steady flow in a fully filled pipeline with constant cross-section is calculated based on the Bernoulli equation. The hydraulic diameter is expressed using the cross-sectional area ($A$) and wetted perimeter ($p$) of the pipe-flow element as follows: $D_h = \frac{4A}{p}$. The flow equation between two points within the element is given as follows [22]:

$$\Delta P - \rho g \Delta Z = C_L \frac{\rho V^2}{2} fL \tag{1}$$

In the equation: $\Delta P$ represents the pressure difference between two nodes (Pa); $\Delta Z$ denotes the elevation difference between two nodes (m); $V$ indicates the flow velocity in the pipeline (m/s); $\rho$ stands for the fluid density in the pipe (kg/m$^3$); $g$ corresponds to gravitational acceleration (m/s$^2$); $C_L = \frac{fL}{D_h}$ signifies the loss coefficient; $f$ refers to the pipeline friction coefficient; $L$ is the pipeline length (m).

*Pipe Flow Unit Verification*

Before formal simulation, the reliability of pipe flow elements is verified. The verification model adopts a U-shaped pipeline, including horizontal and vertical pipe sections, and the bottom is connected by pipe coupling elements. Node A and Node D are located on the ground surface; Node B and Node C are 4000 m underground. The horizontal pipe length is 0.4 m, and the inner diameter is 0.1 m. A constant inlet flow rate of 0.04 m$^3$/s is set at Node A, and the gauge pressure of Node A and Node D is 0. The test fluid is an incompressible liquid with density of 1.2 g/cm$^3$ and viscosity of 1 cP. Since the fluid is incompressible, the flow velocity in the pipeline remains stable, and the pressure of each node can be calculated by the Bernoulli equation. Fig. 1a and 1b shows the numerical calculation results, which are highly consistent with the analytical solutions in Table 1. The verification proves that the pipe flow element can accurately simulate pipeline fluid flow.

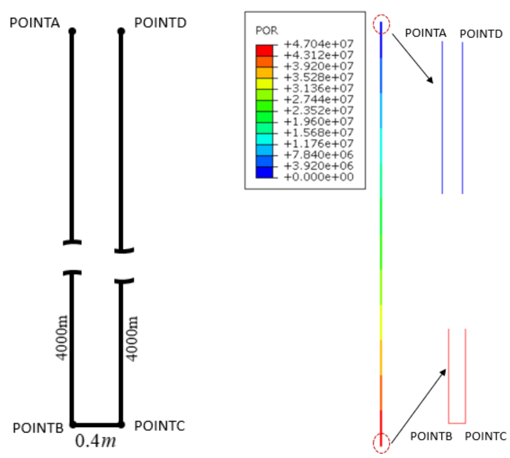


**(a)** **(b)**

**Figure 1:** (**a**) Geometric structure of U-shaped tube; (**b**) Numerical model results.

**Table 1:** Analytic solution of Bernoulli equation.

| Node ID | POR |
|---|---|
| POINTA | 0 |
| POINTB | 47.04 MPa |
| POINTC | 47.04 MPa |
| POINTD | 0 |

## *2.2 Cohesive Unit*

This study employs cohesive zone elements to characterize fracture initiation and propagation behavior, adopting the traction-separation law as the fracture initiation criterion. The traction-separation law, illustrated in Fig. 2, consists of three distinct phases: the pre-damage elastic phase, damage initiation phase, and damage evolution phase. In the initial state, the fracture interface remains closed with intact mechanical properties, exhibiting linear elastic behavior where the interface stiffness remains constant. Under external load, cohesive elements first experience elastic deformation with constant stiffness. Damage initiation is triggered when the load meets the tensile strength criterion, followed by progressive stiffness degradation in the subsequent damage evolution phase. With continued loading, the fracture progressively propagates until complete failure occurs, resulting in the formation of a discrete fracture.

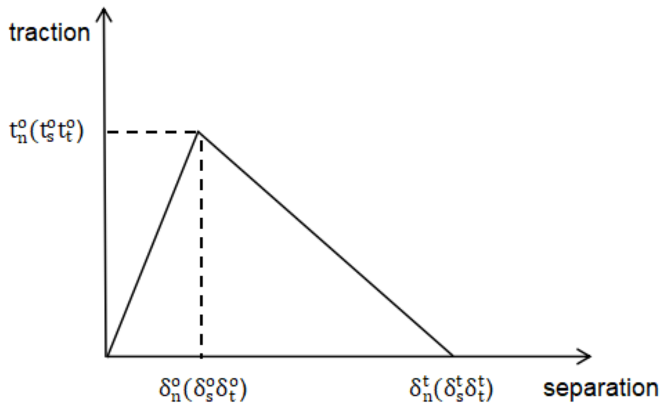


**Figure 2:** Damage criterion diagram of traction separation law.

The quadratic stress criterion is adopted to determine whether fractures initiate [23]:

In the formula: $t_n$, $t_s$, $t_t$ are the stress in the normal direction, the first shear direction and the second shear direction, Pa; $t_n^0$, $t_s^0$ and $t_t^0$ are the normal tensile strength, the shear strength in the first shear direction and the second shear direction, Pa, respectively. $\langle t_n \rangle$ indicates that there is no damage when the element is under pressure.

The normal stress and shear stress within fractures can be characterized as [24]:

$$\boldsymbol{t}_n = \begin{cases} (1-D)\bar{\boldsymbol{t}}_n & \bar{\boldsymbol{t}}_n > 0 \quad (\textit{Tensile stress state}) \\ \bar{\boldsymbol{t}}_n & (\textit{Compressive stress state}) \end{cases} \tag{2}$$

$$\begin{cases} \boldsymbol{t}_s = (1-D)\bar{\boldsymbol{t}}_s \\ \boldsymbol{t}_t = (1-D)\bar{\boldsymbol{t}}_t \end{cases} \tag{3}$$

In the formula, $\bar{\boldsymbol{t}}_n$, $\bar{\boldsymbol{t}}_s$ and $\bar{\boldsymbol{t}}_t$ are the stress components predicted according to the elastic traction separation behavior of the current non-destructive strain, $\boldsymbol{t}_n$, $\boldsymbol{t}_s$ and $\boldsymbol{t}_t$ are the actual stresses in the three corresponding directions, and $D$ is the dimensionless factor.

When the quadratic function value of the traction-separation law reaches unity, damage initiation occurs and the process enters the damage evolution phase. This study adopts the B-K (Benzeggagh-Kenane) energy criterion to govern the damage evolution stage, expressed as follows [25]:

$$G_n^C + (G_S^C - G_n^C)\left(\frac{G_S}{G_T}\right)^{\beta} = G^C \tag{4}$$

Among them, $G_S = G_s + G_t$ is the total energy dissipated in the first and second shear directions;

$G_T = G_n + G_s + G_t$, which is the total energy dissipated in the normal, first and second shear directions;

$G^C = G_n^C + G_s^C + G_t^C$ which is the total energy of critical fracture in the normal, first and second shear directions;

$G_n$, $G_S$ and $G_t$ are the energy dissipated by deformation in the normal, first and second shear directions, respectively;

$G_n^C$, $G_s^C$ and $G_t^C$ are the critical energy required for complete damage in the normal, first and second shear directions, respectively.

### *2.3 Fluid-Solid Interaction Theory (FSI Theory)*

Assuming the formation to be an isotropic poroelastic medium, the coupled pore pressure and porous medium deformation theory is employed to simulate formation deformation and fluid flow within formation pores during dynamic drilling processes.

Based on the principle of virtual work, the stress equilibrium of the solid phase in porous media can be expressed as [21]:

$$\int_V (\bar{\boldsymbol{\sigma}} - \boldsymbol{p}_w \boldsymbol{I}) \boldsymbol{\delta}_\varepsilon \mathrm{d}V = \int_s \boldsymbol{t} \boldsymbol{\delta}_\mathrm{v} \mathrm{d}S + \int_V \boldsymbol{f} \boldsymbol{\delta}_\mathrm{v} \mathrm{d}V \tag{5}$$

where: $\bar{\boldsymbol{\sigma}}$ is the total stress, $\mathrm{Pa}$; $\boldsymbol{p}_w$ is pore pressure, $\mathrm{Pa}$; $\boldsymbol{I}$ is the unit matrix; $\boldsymbol{\delta}_\varepsilon$ is the virtual strain velocity matrix, $\mathrm{s}^{-1}$; $\boldsymbol{\delta}_\mathrm{v}$ is the virtual velocity matrix, $\mathrm{m/s}$; $\boldsymbol{t}$ is the surface force per unit area, $\mathrm{N/m^2}$; $\boldsymbol{f}$ is the physical strength per unit volume, $\mathrm{N/m^3}$; $\mathrm{d}S$ is the area micro-element: $\mathrm{m^2}$; $\mathrm{d}V$ it is a volume element, $m^3$.

The fluid flow within fractures can be decomposed into two fundamental components as illustrated in Fig. 3 [22]:

$$\frac{\partial w}{\partial t} + \nabla q + (\boldsymbol{q}_t + \boldsymbol{q}_b) = 0 \tag{6}$$

In the formula: $q$ is the tangential flow flux, $\mathrm{m^2/s}$; $w$ is the crack width, $\mathrm{m}$; $\boldsymbol{q}_t$ and $\boldsymbol{q}_b$ are the normal filtration velocity of the top and bottom of the fracture, respectively, $\mathrm{m/s}$.

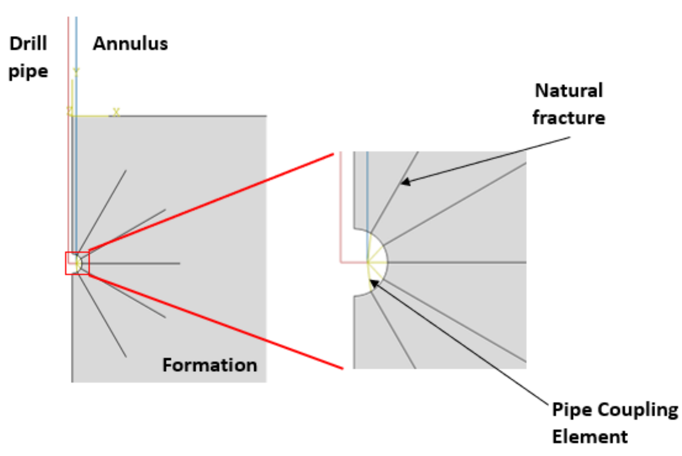


**Figure 3:** Schematic diagram of drilling fluid circulation loss model.

The tangential flow within fractures is mathematically expressed as follows [26]:

$$q = -\frac{w^3}{12\mu_1} \nabla \boldsymbol{p}_f \tag{7}$$

In the formula: $\mu_1$ is the fluid viscosity, $\mathrm{mPa \bullet s}$, $\boldsymbol{p}_f$ is the fluid pressure, $\mathrm{Pa}$.

## 3 Model Building

### *3.1 Geometric Model*

The drilling fluid circulation loss model is illustrated in Fig. 3. The formation dimensions are 25 m × 25 m, with a well depth of 4000 m. The overburden rock pressure is applied along the *Z*-direction (perpendicular to the screen), while the maximum and minimum horizontal principal stresses are set along the *X* and *Y* directions, respectively. To reduce computational cost, improve convergence, and enhance calculation accuracy, a half-formation model is established.

The formation is modeled using a linear elastic material with coupled pore pressure and displacement, while fractures are represented by cohesive zone elements incorporating coupled pore pressure and displacement. The drill pipe (left) and annulus (right) are characterized using U-shaped pipe structures constructed with Fluid Pipe Elements (FPEs). Although the dimensions of the U-shaped pipe are fixed, different wellbore configurations can be equivalently simulated by adjusting parameters such as the friction factor.

### *3.2 Boundary Condition*

The left boundary of the model adopts symmetric constraints, while a predefined initial pore pressure field is established within the formation medium. Displacement restrictions and pore pressure boundaries are applied along both the *y*-axis and *x*-axis directions to ensure mechanical equilibrium.

In the wellbore region, gravitational loading is applied to simulate the hydrostatic pressure of the drilling fluid column. The top of the drill pipe is subjected to a fixed-flow-rate inlet condition, while its bottom end achieves pressure coupling with the annulus, wellbore contact surfaces, and fracture pore pressure nodes. The upper boundary of the annulus is set to zero-pressure condition to ensure reasonable pressure gradient distribution.

The wellbore bottom is connected to formation nodes along the wellbore wall and fracture pore pressure nodes, maintaining dynamic consistency between wellbore wall pressure and bottomhole pressure. When intersecting with the wellbore, fracture nodes automatically inherit the bottomhole pressure parameters when fractures are open. By establishing a pressure transmission pathway among the drill pipe-formation-fracture system, fluid mass conservation across multiple domains is achieved.

This coupled design accurately simulates the seepage interaction process of drilling fluid within the wellbore, formation pores, and fracture network, ensuring physically realistic fluid dynamic responses.

### *3.3 Model Verification*

In this study, the model verification research was carried out based on the control variable method, and the self-built two-dimensional drilling fluid dynamic leakage model was systematically compared with JIA Lichun Lost Circulation Model [8]. Using the same model input parameters, Table 2:

**Table 2:** Validate model input parameters.

| Parameter | Value | Parameters | Value |
|---|---|---|---|
| x (m) | 100 | ρ (kg/m$^3$) | 1200 |
| y (m) | 100 | K (pa.s$^n$) | 0.5 |
| α | 1 | n | 0.8 |
| $k_n$ (Pa/m) | 5 × $10^{11}$ | $C_t$ (m/s$^{0.5}$) | 5 × $10^{-13}$ |
| θ (°) | 45 | γ | 1 |

| | | | |
|---|---|---|---|
| $w_o$ (mm) | 1 | $P_f$ (MPa) | 40 |
| g (m/s$^2$) | 10 | τ (s) | 0.1 |
| $P_o$ (MPa) | 30 | t (s) | 100 |

The comparative experimental data illustrated in Fig. 4 demonstrate that the numerical model developed in this study exhibits favorable consistency with the JIA model in trend prediction, where the computational deviation between the two models remains within 5%, thereby effectively validating the reliability of the proposed model. Notably, the observed minor discrepancies between models predominantly manifest during the initial dynamic response phase: Compared with the JIA model, the fluid loss rate characterized by our model displays a more pronounced attenuation gradient. Through mechanism analysis, this divergence is attributed to the JIA model's incorporation of a fracture wall roughness correction coefficient in its hydrodynamic equations. This parameter amplifies fluid shear stress, thereby reducing the seepage efficiency of drilling fluid within the fracture system and inducing a time-lag effect during fracture packing. However, from the perspective of overall evolutionary behavior, the systemic differences between the two models remain insignificant, satisfying the simulation accuracy requirements for drilling fluid loss dynamics in engineering practice.

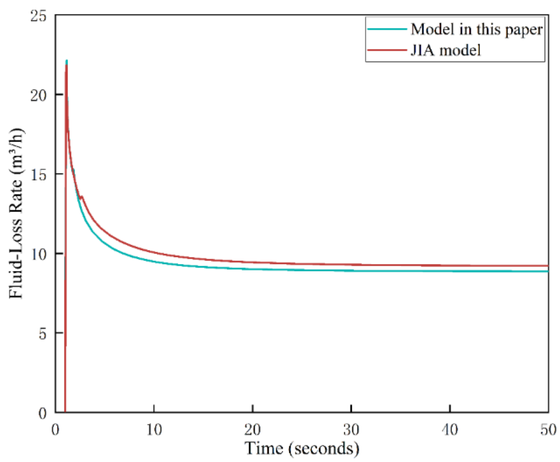


**Figure 4:** Model validation result.

## 4 Influence of Formation Parameters on Drilling Fluid Leakage

This study investigates the dynamic behavior of drilling fluid loss in multi-scale fractured reservoirs under high-permeability formation conditions (permeability of 100 mD). Through maintaining constant fluid loss coefficient and other operational parameters, we systematically examine the governing effects of formation parameters (elastic modulus and Poisson's ratio) on both fluid loss rate and fracture width evolution. Employing the control variable method, quantitative analyses were conducted on: (1) elastic modulus variations within 15–35 GPa range and (2) Poisson's ratio parameter sets spanning 0.1–0.45, elucidating their respective control mechanisms on fluid migration within fracture networks. The coupled interaction mechanisms of different formation parameters in multi-scale fracture systems were rigorously revealed. Furthermore, the differential control mechanisms of fracture aperture and fracture length on fluid loss dynamics were systematically investigated through numerical simulations. Results demonstrate that aperture variations predominantly govern fluid flux through modification of seepage cross-sectional area, while fracture propagation length regulates loss dynamics by modulating pressure gradient distribution. These two factors collectively constitute the governing equations for fluid loss under multi-physics coupling effects.

### *4.1 Elastic Modulus*

As shown in Fig. 5, the fluid loss rate decreases with increasing formation elastic modulus. When the elastic modulus rises from 15 GPa to 35 GPa, the peak loss rate declines from 13.75 $m^3/h$ to 13.55 $m^3/h$, representing a reduction of 1.5%. This trend occurs because high-modulus formations exhibit greater rigidity, resulting in narrower fracture apertures that restrict fluid flow pathways and consequently reduce leakage velocity. Conversely, low elastic modulus formations are more deformable, allowing fractures to propagate rapidly and develop wider flow channels, thereby leading to higher peak loss rates.

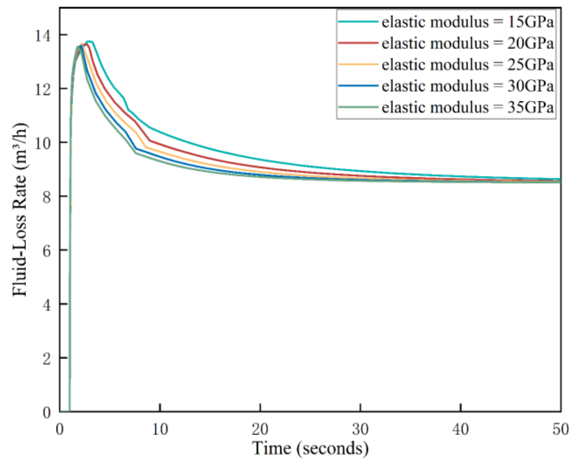


**Figure 5:** Effect of elastic modulus on drilling fluid leakage.

Fig. 6 illustrates the influence of formation elastic modulus on fracture aperture width. Numerical simulation results demonstrate a significant negative correlation between fracture width and formation elastic modulus: when the elastic modulus increases from 15 GPa to 35 GPa, the fracture width decreases from 3.33 mm to 1.68 mm, representing a reduction of 49.5%. This phenomenon occurs because under identical drilling fluid pressure conditions, fracture walls in high-elastic-modulus formations exhibit limited elastic expansion capacity, thereby constraining fracture opening. In contrast, formations with low elastic modulus develop wider fracture channels due to their greater elastic deformation capacity.

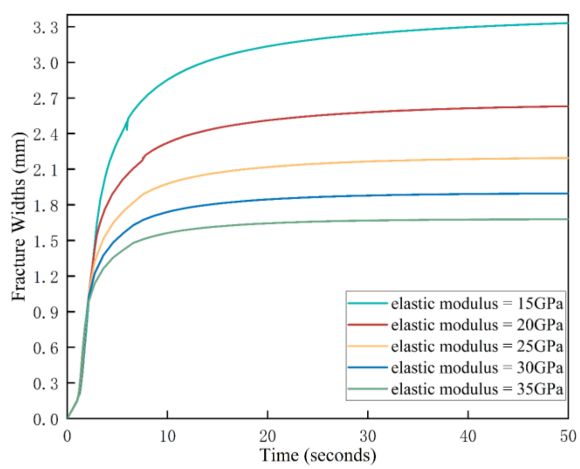


**Figure 6:** Effect of elastic modulus on crack mouth width.

### *4.2 Poisson's Ratio*

Fig. 7 demonstrates the effect of formation Poisson's ratio on drilling fluid loss rate. The results reveal that during the initial wellbore fracture stage, the fluid loss rate decreases with increasing Poisson's ratio, while the loss rates converge during the equilibrium stage. When Poisson's ratio increases from 0.1 to 0.45, the peak loss rate declines from 14.6 $m^3/h$ to 8.61 $m^3/h$, representing a 41.3% reduction. This occurs because formations with higher Poisson's ratios exhibit stronger lateral expansion effects in the rock, which suppresses rapid fracture initiation and consequently reduces the peak loss rate. During the equilibrium stage, when fractures have fully propagated, the loss rate becomes primarily governed by fracture geometry and pressure gradient. At this point, the direct influence of Poisson's ratio on fracture aperture diminishes, leading to convergent loss rates.

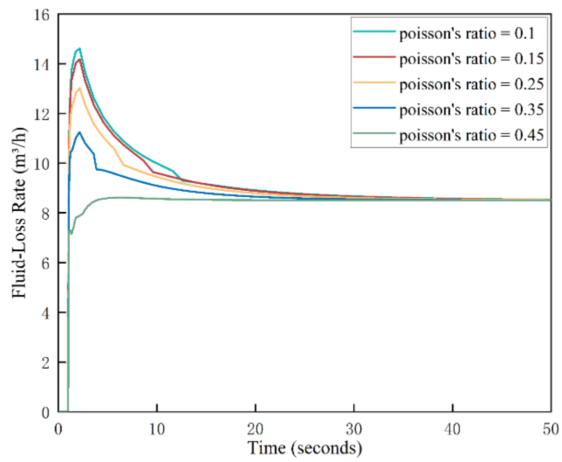


**Figure 7:** Effect of Poisson's ratio on drilling fluid leakage.

Fig. 8 demonstrates the regulatory effect of Poisson's ratio on fracture aperture width. Numerical simulation results reveal a positive correlation between fracture aperture and Poisson's ratio: when Poisson's ratio increases from 0.1 to 0.45, the fracture width significantly expands from 1.78 mm to 2.5 mm, representing a relative increase of 40.4%. This phenomenon occurs because formations with higher Poisson's ratios exhibit enhanced transverse strain capacity during fracturing processes, resulting in reduced normal stress on fracture surfaces and consequently facilitating the formation of wider fractures.

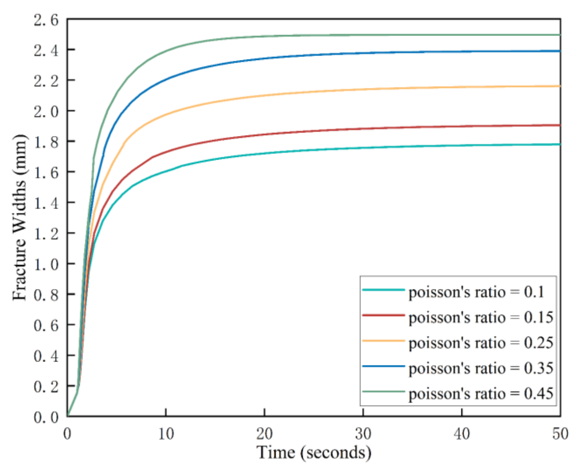


**Figure 8:** Effect of Poisson's ratio on crack mouth width.

### *4.3 Fracture Length*

Fig. 9 demonstrates the influence of fracture length on drilling fluid loss rate under constant fluid loss coefficient conditions. As fracture length increases from 5 m to 15 m, the stabilized loss rate during dynamic equilibrium phase rises from 0.53 $m^3/h$ to 1.24 $m^3/h$ (a 133.9% increase). This phenomenon can be attributed to two key mechanisms governing fluid flow in multi-fracture systems:

(1) Temporal Effect: Longer fractures require extended time for complete drilling fluid filling, resulting in slower pressure transmission and consequently more gradual loss rate reduction.

(2) Geometric Effect: During stabilized filtration, longer fractures maintain higher loss rates due to their increased surface area (directly proportional to fracture length), which enhances filtration capacity.

The coupling of these mechanisms explains why fracture networks with greater lengths exhibit significantly higher stabilized loss rates compared to shorter fracture systems.

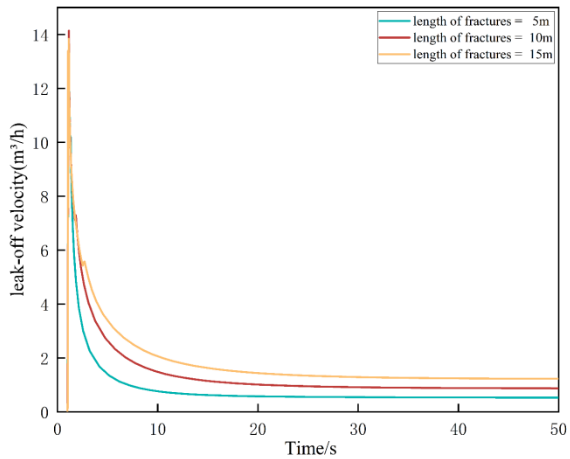


**Figure 9:** Effect of fracture length on drilling fluid leakage.

As shown in Fig. 10, the fracture aperture width decreases with increasing fracture length. This phenomenon occurs because shorter fractures are rapidly filled with drilling fluid, leading to selective accumulation near the fracture entrance. Numerical simulation results demonstrate that when fracture length increases from 5 m to 15 m, the final equilibrium aperture width decreases from 11.5 mm to 9.6 mm (a 19.8% reduction).

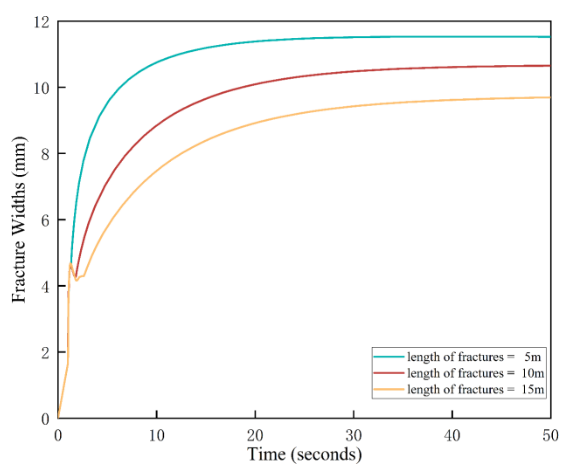


**Figure 10:** Effect of fracture length on fracture aperture.

### *4.4 Fracture Aperture*

Fracture aperture determines formation permeability and leakage channel scale, which is the key factor affecting leakage type, loss rate and wellbore stability. Large-aperture fractures are easy to induce severe leakage, even blowout and wellbore collapse. For formations with multi-scale fractures, the leakage problem is more complex. This paper designs 4 groups of fracture aperture distribution schemes (Table 3), and 5 fractures are arranged circumferentially around the wellbore in each scheme.

Scheme design explanation: Four groups of schemes are designed to cover micron-millimeter multi-scale mixed fractures and single millimeter-scale fractures, which can compare the leakage difference between micro-fractures and macro-fractures, and clarify the dominant leakage channel in multi-fracture system.

**Table 3:** Different crack opening configuration simulation schemes.

| Serial Number | Fracture Aperture |
|---|---|
| Case 1 | 10 μm/200 μm/700 μm/1 mm/2 mm |
| Case 2 | 2 mm/400 μm/700 μm/1 mm/500 μm |
| Case 3 | 100 μm/300 μm/500 μm/700 μm/900 μm |
| Case 4 | 9 mm/7 mm/5 mm/3 mm/1 mm |

Fig. 11 illustrates the evolution characteristics of formation pressure over time under different scenarios, with all cloud diagrams standardized using a unified color scale. Analysis reveals that in Scenario 1 and Scenario 2, a multi-scale fracture system ranging from micron-level to millimeter-level develops around the wellbore. During the initial stage of lost circulation, drilling fluid preferentially invades the formation rapidly through major fracture channels with millimeter-scale widths, subsequently gradually diffusing into secondary microfractures (micron-scale). The fracture network in Scenario 4 exhibits millimeter-scale fracture apertures. Due to stress interference effects among fracture clusters, the central fractures form localized high-stress barriers under the compressive constraints from adjacent fractures, significantly delaying the initial invasion rate of drilling fluid. However, as time progresses, dynamic adjustments in the stress field facilitate sequential interconnection of fractures, ultimately resulting in all fractures participating in the lost circulation process. Notably, the differences in conductivity among various fractures lead to markedly heterogeneous distribution of fluid loss, creating a complex pressure field characterized by alternating local high-pressure and low-pressure zones.

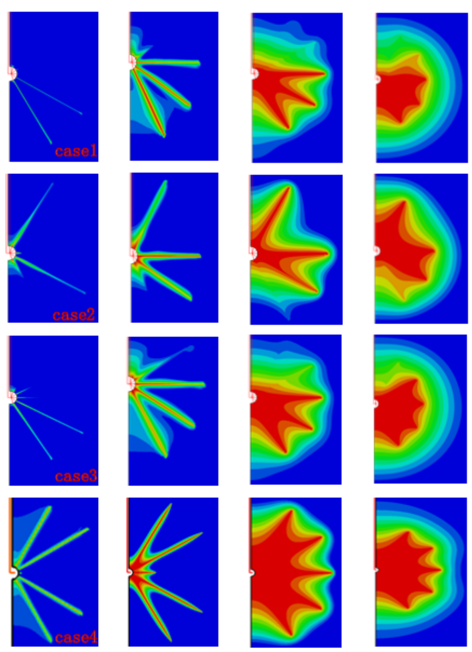


**Figure 11:** The change of formation pressure with time in different schemes.

Fig. 12 shows the leakage characteristics of Case 4 (single millimeter-scale fractures). The peak loss rate increases linearly with fracture aperture. When aperture increases from 1 mm to 9 mm, peak loss rate rises from 11.86 $m^3$/h to 12.61 $m^3$/h, with an increase of 6.32%. The growth amplitude is small due to multi-fracture competition: wide fractures form dominant leakage channels at the initial stage, while narrow fractures are delayed due to large flow resistance. After the fractures are fully filled, leakage is mainly controlled by fracture wall filtration.

Considering the cubic relationship between fracture flow rate and aperture, the peak leakage rate is less sensitive to aperture changes, which seems counterintuitive. This difference can be explained by two competing mechanisms inherent in the fluid-solid coupling framework: Flow resistance transition: In the single-fracture system of Case 4, after the fracture space is completely filled with drilling fluid, the main flow resistance rapidly shifts from viscous dissipation within the fracture to filtration at the fracture wall. Once filtration dominates, the leakage rate is controlled by the permeability of the filter cake and the properties of the fracture wall, rather than the aperture size. Pressure boundary constraint: The wellbore pressure is dynamically coupled with the fracture inlet. As the aperture increases, the pressure required to maintain a given flow rate decreases, thereby reducing the driving force for fracture opening. This negative feedback loop formed through fluid-solid coupling effectively decouples the leakage rate from the cubic relationship with aperture predicted by the ideal slit flow theory. These findings emphasize that in a dynamically coupled system, the simple hydraulic aperture-flow rate relationship may not hold, and fluid-solid interaction must be considered for accurate prediction.

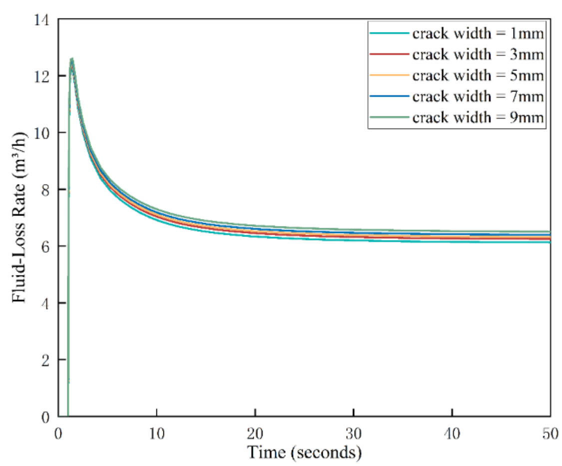


**Figure 12:** Case 4: Leakage velocity changes with time.

Fig. 13 shows the leakage characteristics of Case 1 (micron-millimeter mixed fractures). Peak loss rate increases linearly with aperture. When aperture expands from 10 μm to 2 mm, peak loss rate rises from 0.91 $m^3$/h to 16.23 $m^3$/h, with an increase of 1683.5%. It is found that the loss rate of fractures smaller than 200 μm is close to zero, which can be ignored in engineering.

Supplementary explanation of critical threshold: 200 μm is the critical size of effective leakage. When the aperture is less than 200 μm, the flow resistance of drilling fluid is extremely large under the action of capillary force and fluid viscosity, and the fluid is difficult to flow; when the aperture exceeds 200 μm, capillary force is weakened, fluid flow resistance decreases sharply, and obvious leakage is formed.

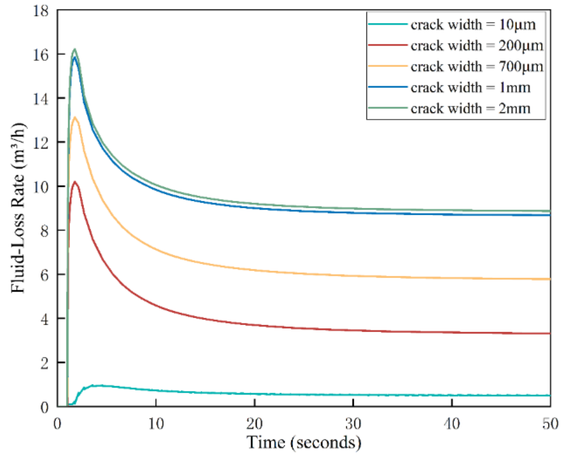


**Figure 13:** Case 1: Leakage velocity changes with time.

## 5 Influence of *in-Situ* Stress Parameters on Drilling Fluid Loss

Fig. 14 shows the influence of maximum-minimum horizontal principal stress difference on loss rate. Peak loss rate increases with the rise of stress difference. When stress difference increases from 5 MPa to 25 MPa, peak loss rate rises from 13.65 $m^3$/h to 16.22 $m^3$/h, with an increase of 18.83%. Stress difference determines the severity of leakage in the early stage. In the later stable stage, the loss rate of all groups converges to a similar level.

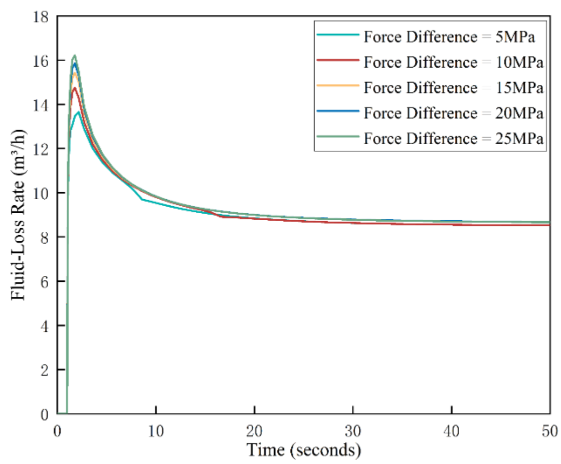


**Figure 14:** Effect of *in-situ* stress difference on drilling fluid leakage.

Fig. 15 shows the variation of fracture aperture under different stress difference. Fracture width is negatively correlated with stress difference. When stress difference increases from 5 MPa to 25 MPa, fracture width decreases from 2.03 mm to 1.28 mm, with a reduction of 36.9%. Larger stress difference produces stronger lateral compression on fracture surface, which restricts fracture opening.

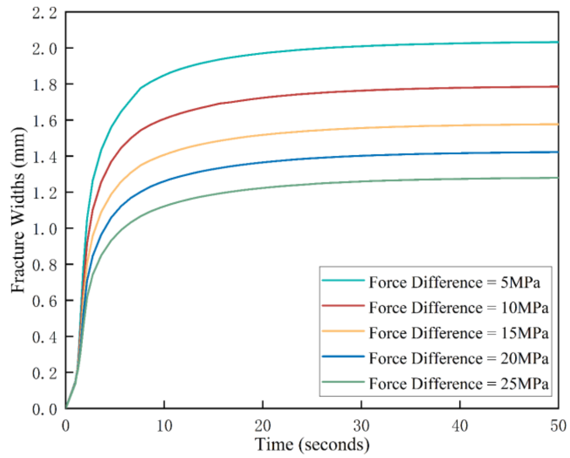


**Figure 15:** Effect of *in-situ* stress on fracture aperture.

## 6 The Influence of Engineering Parameters on Drilling Fluid Leakage

Taking the high-permeability formation (100 mD) as the research object, this section studies the influence of pump rate, drilling fluid density and viscosity on loss rate and fracture aperture via control variable method, and reveals the coupling law of engineering parameters in multi-scale fracture system.

### *6.1 Flow Rate*

Under the condition of fixed fracture parameters and fluid properties, Fig. 16 shows the influence of pump rate on loss rate. When flow rate increases from 0.03 $m^3/s$ to 0.05 $m^3/s$, peak loss rate rises from 14.94 $m^3/h$ to 16.71 $m^3/h$ (increase by 11.8%), and stable loss rate rises from 8.01 $m^3/h$ to 9.55 $m^3/h$ (increase by 19.2%). Flow rate is positively correlated with loss rate, which is a key control parameter in drilling engineering. Reasonable flow rate can balance cuttings carrying, leakage control and operation economy.

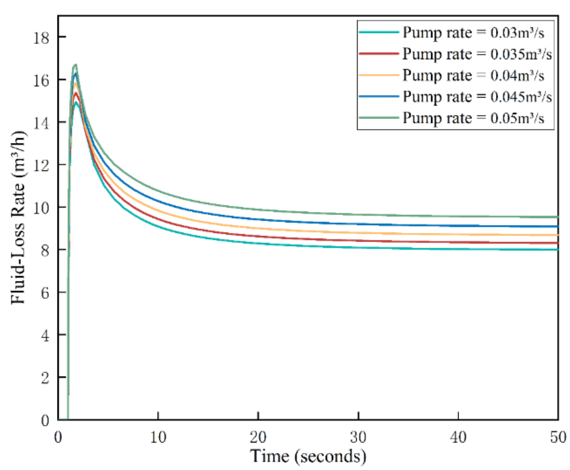


**Figure 16:** Effect of pump rate on drilling fluid leakage.

Fig. 17 shows the dynamic evolution of fracture aperture. At the initial stage of formation breakdown, a large amount of fluid invades the formation, and fracture aperture expands rapidly; then the expansion speed slows down and finally tends to be stable. When flow rate increases from 0.03 $m^3/s$ to 0.05 $m^3/s$, stable fracture aperture rises from 1.23 mm to 1.66 mm, with an increase of 35%. In field construction, flow rate should be controlled within a reasonable range to avoid excessive fracture propagation.

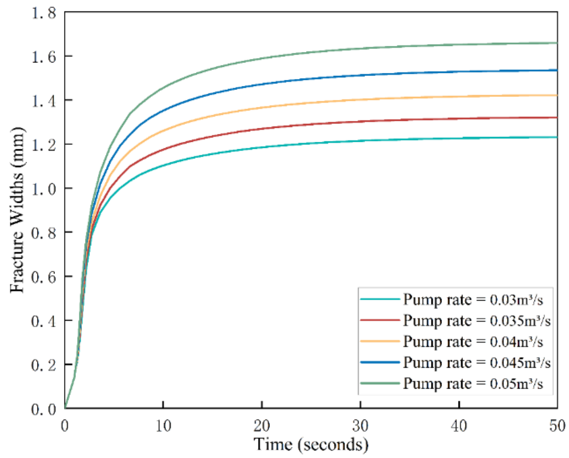


**Figure 17:** Effect of pump rate on fracture aperture.

### *6.2 Density*

Fig. 18 shows the influence of drilling fluid density on leakage. When density increases from 0.8 g/cm$^3$ to 1.6 g/cm$^3$, peak loss rate rises from 12.23 m$^3$/h to 18.03 m$^3$/h (increase by 47.4%). Drilling fluid density changes the pressure difference between wellbore and formation via hydrostatic pressure, and further affects fracture propagation and leakage degree. For fractured formations, it is necessary to formulate a reasonable density control window based on formation fracture pressure.

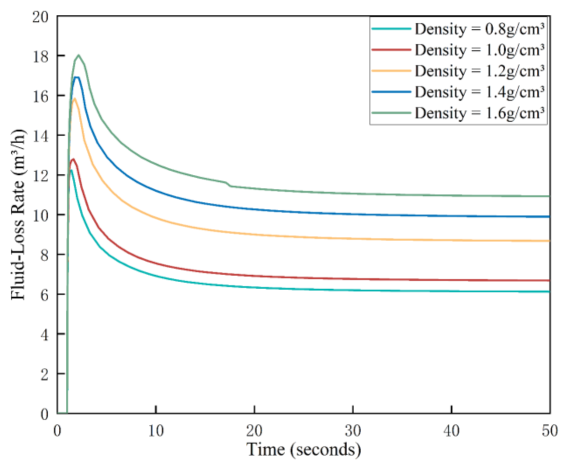


**Figure 18:** Effect of fluid density on drilling fluid leakage.

Fig. 19 shows the relationship between density and fracture aperture. When density increases from 0.8 g/cm$^3$ to 1.6 g/cm$^3$, stable fracture aperture expands from 0.73 mm to 2.04 mm, with an increase of 179.5%. Higher fluid density leads to larger bottomhole pressure, which promotes fracture opening significantly.

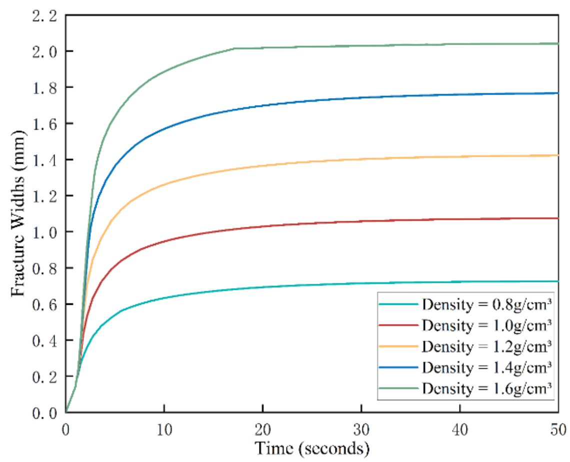


**Figure 19:** Effect of density on crack mouth width.

### *6.3 Viscosity*

Fig. 20 shows the staged influence of fluid viscosity on loss rate. At the fracture initiation stage, when viscosity increases from 20 mPa·s to 40 mPa·s, peak loss rate decreases from 15.99 $m^3$/h to 15.72 mPa·s (reduction by 1.7%). Higher viscosity increases flow resistance, inhibits fracture initiation and reduces initial leakage. At the stable stage, the rule is reversed: high-viscosity fluid needs larger pressure gradient to maintain flow, which promotes fracture expansion, so stable loss rate increases with viscosity.

Explanation of two-stage regulation mechanism: The flow resistance of high-viscosity fluid is large. In the stage of fracture initiation (small fracture aperture), high viscosity can hinder fluid invasion and suppress leakage; after the fracture expands and enters the stable seepage stage, the fluid cannot flow smoothly under high viscosity, which will continuously squeeze the fracture wall to make the aperture larger, and finally lead to the increase of stable loss rate.

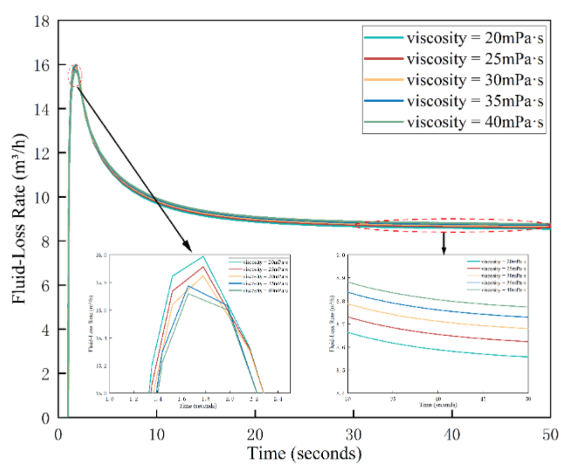


**Figure 20:** Effect of viscosity on drilling fluid leakage.

Fig. 21 shows the evolution of fracture aperture under different viscosity. At the initial stage, fracture width decreases with the increase of viscosity; at the stable stage, fracture width increases slightly. When viscosity rises from 20 mPa·s to 40 mPa·s, stable aperture increases from 1.39 mm to 1.45 mm, with an increase of 4.3%. This phenomenon fully reflects the dynamic characteristics of fluid-solid coupling in the whole fracturing process.

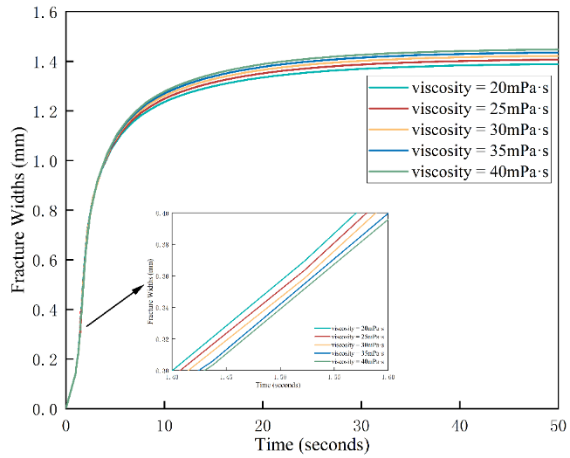


**Figure 21:** Effect of viscosity on fracture mouth width.

## 7 Conclusion

Aiming at the leakage control problem of multi-scale fractured formations in deep well drilling, this paper establishes a dynamic finite element model based on fluid-solid coupling theory and systematically studies the coupling mechanism of fracture propagation and leakage channel evolution. By combining pipe flow elements and cohesive zone elements, the influences of engineering parameters, fracture geometric parameters, and geomechanical parameters on loss rate and fracture aperture are analyzed. The main conclusions are summarized as follows:

(1) Pump rate and drilling fluid density are positively correlated with fluid loss rate and fracture aperture. When flow rate increases from 0.03 $m^3/s$ to 0.05 $m^3/s$, the stable loss rate increases by 19.2%, and the stable fracture aperture increases by 35%.

(2) Drilling fluid viscosity presents an obvious two-stage regulation effect: it restricts leakage at the fracture initiation stage and aggravates leakage in the steady-state stage.

(3) Fracture length has little influence on initial loss rate; longer fracture corresponds to slower attenuation of loss rate. Fractures with aperture larger than 200 μm are the main leakage channels, and loss rate increases with aperture.

(4) Fluid loss rate decreases with the increase of formation elastic modulus and Poisson's ratio, and increases with the rise of *in-situ* stress difference. When Poisson's ratio increases from 0.1 to 0.45, peak loss rate decreases by 41.3%.

(5) Fracture aperture decreases with the increase of elastic modulus and *in-situ* stress difference, and increases with the rise of Poisson's ratio. When stress difference increases from 5 MPa to 25 MPa, fracture aperture decreases by 36.9%.

**Acknowledgement:** Not applicable.

**Funding Statement:** This research work was supported by the Research on Key Technologies for Deep Thick Salt Layer Storage XAI (2025DJ8309), the Research on the Complex Geological Multi-Wellbore Injection and Production Mode of Underground Salt Cavern Compressed Air Energy Storage (2024DQ03181) and the CNPC Research Institute of Engineering Technology Co., Ltd., Project (CPET202511).

**Author Contributions:** Pan Fu: Data Curation, Formal Analysis, Visualization. Yueyang Guan: Writing—Review & Editing, Project Administration. Qi He: Software, Validation, Investigation. Jiangshuai Wang: Supervision, Funding

Acquisition, Resources. Bohan Zheng: Conceptualization, Methodology, Writing—Original Draft. All authors reviewed and approved the final version of the manuscript.

**Availability of Data and Materials:** The data and materials used in this study, including numerical simulation models, Abaqus input files, and user-defined subroutines, are available from the corresponding author upon reasonable request.

**Ethics Approval:** This study does not involve any human or animal subjects, and no ethical approval is required. Not applicable.

**Conflicts of Interest:** Given his/her role as Guset Editor of this journal,Pan Fu and Jiangshuai Wang had no involvement in the peer review of this article and had no access to information regarding its peer review. Full responsibility for the editorial process for this article was delegated to another journal editor. The authors declare no other conflicts of interest.

## References

1. Huang G, Yin F, He H, Zeng P. Intelligent prediction of lost circulation based on improved k-nearest neighbor and self-attention mechanism-convolutional neural network. Geoenergy Sci Eng. 2025;247:213712. doi:10.1016/j.geoen.2025.213712.
2. Nazemi R, Zargar G, Nooripoor V. Experimental investigation of deformable additives as loss circulation control agent during drilling and well construction. Sci Rep. 2024;14(1):30423. doi:10.1038/s41598-024-66208-5.
3. Li P, Ru D, Wang J, Yin L, Bo Z, Ye Y, et al. Discussion on the technology of leak prevention and sealing in drilling engineering. J Phys Conf Ser. 2024;2834(1):012035. doi:10.1088/1742-6596/2834/1/012035.
4. Miranda CR, Oliveira JL, Cavalcante GM, D'Almeida AR, Pereira RF, Santos RL, et al. Materials for controlling severe lost circulation-laboratory evaluation. In: Proceedings of the SPE Latin America and Caribbean Petroleum Engineering Conference; 2017 May 17–19; Buenos Aires, Argentina. doi:10.2118/185582-ms.
5. Feng Y, Gray KE. Lost circulation and wellbore strengthening. Cham, Switzerland: Springer International Publishing; 2018. doi:10.1007/978-3-319-89435-5.
6. Fidan E, Babadagli T, Kuru E. Use of cement as lost circulation material-field case studies. In: Proceedings of the IADC/SPE Asia Pacific Drilling Technology Conference and Exhibition; 2004 Sep 13–15; Kuala Lumpur, Malaysia. p. SPE 88005–MS. doi:10.2118/88005-ms.
7. Lavrov A. Lost circulation: Mechanisms and solutions. Burlington, MA, USA: Gulf Professional Publishing; 2016.
8. Jia L, Chen M, Hou B, Sun Z, Jin Y. Drilling fluid loss model and loss dynamic behavior in fractured formations. Petrol Explor Dev. 2014;41(1):105–12. doi:10.1016/S1876-3804(14)60012-4.
9. Lietard O, Unwin T, Guillot D, Hodder M. Fracture width LWD and drilling mud/LCM selection guidelines in naturally fractured reservoirs. In: Proceedings of the European Petroleum Conference; 1996 Oct 22–24; Milan, Italy. p. SPE 36832–MS. doi:10.2118/36832-ms.
10. Li DQ, Kang YL, Liu XS, Chen ZW, Si N. Progress in drilling fluid loss dynamics model for fractured formations. Pet Drill Tech. 2013;41(4):42–7. (In Chinese). doi:10.3969/j.issn.1001-0890.2013.04.010.
11. Du H, Feng J, Xu S, Qu J, Li C, Gao X, et al. Quantitative prediction of tertiary formation fractures and its application in lost circulation prediction in the Bozhong Depression. Geomech Energy Environ. 2025;44:100749. doi:10.1016/j.gete.2025.100749.
12. Lavrov A, Tronvoll J. Numerical analysis of radial flow in a natural fracture: Applications in drilling performance and reservoir characterization. In: Proceedings of the Abu Dhabi International Petroleum Exhibition and Conference; 2006 Nov 5–8. Abu Dhabi, UAE. doi:10.2118/103564-ms.
13. Lavrov A. Newtonian fluid flow from an arbitrarily-oriented fracture into a single sink. Acta Mech. 2006;186(1):55–74. doi:10.1007/s00707-006-0324-9.
14. Salehi S. Numerical simulations of fracture propagation and sealing: Implications for wellbore strengthening [dissertation]. Rolla, MO, USA: Missouri University of Science and Technology; 2012.
15. Feng Y, Gray KE. Modeling lost circulation through drilling-induced fractures. SPE J. 2018;23(1):205–23. doi:10.2118/187945-pa.
16. Feng Y, Arlanoglu C, Podnos E, Becker E, Gray KE. Finite-element studies of hoop-stress enhancement for wellbore strengthening. SPE Drill Complet. 2015;30(1):38–51. doi:10.2118/168001-pa.
17. Zhang S, Feng YC, Gu CW, Deng JG. Study on influence of temperature on loss of drilling fluid based on ABAQUS. China Petrol Mach. 2023;51(7):10–8. (In Chinese). doi:10.16082/j.cnki.issn.1001-4578.2023.07.002.

18. Shen CL, Zhang LL, Liu H, Wang BQ. Numerical simulation analysis of a strengthening method for shear capacity of a voided slab bridge using finite element software ABAQUS. Int J New Dev Eng Soc. 2023;7(2):22–7. doi:10.25236/ijndes.2023.070205.
19. Qiu Y, Ma T, Peng N, Liu J, Ranjith PG. Fully coupled anisotropic porothermoelasticity modeling for inclined borehole in shale formations. Rock Mech Rock Eng. 2024;57(1):597–619. doi:10.1007/s00603-023-03569-9.
20. Zhang GM, Liu H, Zhang J, Wu HA, Wang XX. Three-dimensional finite element simulation and parametric study for horizontal well hydraulic fracture. J Petrol Sci Eng. 2010;72(3–4):310–7. doi:10.1016/j.petrol.2010.03.032.
21. Peirce A, Detournay E. An implicit level set method for modeling hydraulically driven fractures. Comput Meth Appl Mech Eng. 2008;197(33–40):2858–85. doi:10.1016/j.cma.2008.01.013.
22. Batchelor GK. An introduction to fluid dynamics. Cambridge, UK: Cambridge University Press; 2000. doi:10.1017/cbo9780511800955.
23. Soliman MY, Rezaei A, Khalaf M, Gordon P, Cipolla C. Pulse power plasma stimulation: A technique for waterless fracturing, enhancing the near wellbore permeability, and increasing the EUR of unconventional reservoirs. Gas Sci Eng. 2024;122:205201. doi:10.1016/j.jgsce.2023.205201.
24. Zoback MD. Reservoir geomechanics. Cambridge, UK: Cambridge University Press; 2007. doi:10.1017/cbo9780511586477.
25. Liu S, Wang Y, Peng C, Wu W. A thermodynamically consistent phase field model for mixed-mode fracture in rock-like materials. Comput Meth Appl Mech Eng. 2022;392:114642. doi:10.1016/j.cma.2022.114642.
26. Chen S, Wang R, Hou Y, Wang Z, Pan X, Zhang Y, et al. Computational fracture mechanics modeling and multivariate analysis of mixed-mode I-II crack propagation in unstable rock masses. Rock Mech Rock Eng. 2026:1–31. doi:10.1007/s00603-026-05564-2.